JOURNAL OF GEOPHYSICAL RESEARCH, VOL. 98, NO. C7, PAGES 12,469–12,482, JULY 15, 1993

The Detectability of Arctic Leads Using Thermal Imagery Under Varying Atmospheric Conditions

ROBERT S. STONE AND JEFFREY R. KEY

Division of Cryospheric and Polar Processes, Cooperative Institute for Research in Environmental Sciences University of Colorado, Boulder

Arctic leads (open or refrozen fractures in sea ice) provide for the exchange of heat between the ice/ocean surface and the atmosphere. Their influence on the energy budget is not easy to quantify, however, because little is known about their spatial and temporal distributions due to the difficulty in detecting and mapping leads using remote sensing techniques. The way in which thermal contrast between leads of varying widths and thicknesses can be distinguished from the background multiyear ice surface under varying atmospheric conditions is examined. The normalized brightness temperature difference between image pixels that include lead fractions and of the background ice is used in an attempt to determine thresholds of detection accounting for sensor field-of-view and various atmospheric phenomena that influence the Arctic radiation balance during winter. Brightness temperatures are derived from modeled top-of-the-atmosphere radiances for three thermal channels (3, 4 and 5) of the Advanced Very High Resolution Radiometer. Surface temperatures are prescribed as a function of ice thickness and the effects of the intervening atmosphere are simulated by varying the optical depths of hypothetical cloud or haze layers varying in microphysical characteristics. Results indicate that the limits of lead detection may be determined as a function of pixel lead fraction and atmospheric optical depth if suitable values of normalized contrast are used as detection criteria. For example, given a pixel resolution of 1.0 km and the presence of a layer of ice crystals having a visible optical depth of 0.6 just above the surface, the minimum detectable lead width is estimated to be between 400 m and 750 m depending on what threshold criteria are used which, in turn, depends on the homogeneity of the multiyear ice surface. For the same conditions and range of threshold criteria but assuming a layer optical depth of 0.3, the minimum detectable lead width decreases to between 290 m and 560 m. Minimum detectable lead widths are also found to depend on the microphysical and physical properties of any intervening atmospheric layer. Our simulations indicate that narrower leads are detectable when hazy conditions exist than when stratiform water or ice clouds are present for any given layer optical depth.

INTRODUCTION

Linear openings in the ice pack, or leads, are an important component of the heat budget of the Arctic. Leads may be a significant source of heat and moisture to the Arctic atmosphere [e.g., *Andreas et al.*, 1979; *Smith et al.*, 1983; *Schnell et al.*, 1989], especially during winter. During summer leads provide a "window" for the penetration of solar radiation thus enhancing the energy stored in the ocean during the sunlit months. The magnitude of their impact on the global climate is difficult to assess, however, without a knowledge of their frequency of occurrence and spatial distribution. The use of remotely sensed thermal images, particularly data collected using the infrared (IR) and near infrared (NIR) channels of the Advanced Very High Resolution Radiometer (AVHRR) onboard the NOAA-series operational satellites, may provide a means to detect and map leads. To date no operational method to do this has been developed. In *Key et al.* [1993] and J. Key et al. (Effects of satellite sensor field of view on the retrieved geometrical characteristics of sea ice leads, submitted to *Remote Sensing of the Environment*, 1993) the effects of varying the field-of-view (FOV) of satellite sensors on our ability to retrieve lead width distributions and total area fraction are examined. Based on an analysis of high resolution Landsat imagery, *Key and Peckham* [1991] conclude that most leads are less than 500 m wide which, unfortunately, is considerably below the resolution of most satellite radiometers. The length of leads are highly variable and depend on regional dynamical forcings by ocean currents and winds. Typically, intersecting lead segments are on the order of tens of kilometers long and intersecting leads may extend for hundreds of kilometers. Whether or not leads are detectable using remote sensing techniques depends not only on their size, however, but also on their surface properties and on how the intervening atmosphere modulates the flow of upwelling radiation.

Here we address the need to understand how different sensors respond radiometrically to varying surface types and intervening atmospheric layers by evaluating the combined use of multispectral image and contrast analyses to determine thresholds of lead detection under varying atmospheric conditions. Our objective is to estimate the narrowest resolvable lead under a given set of surface and atmospheric conditions, sensor FOV and viewing geometry. Although this investigation focuses on the use of AVHRR data, the approach should have general applicability to other thermal sensors of differing spectral response and view characteristics. The modeling results presented here contrast simulations of clear-sky conditions

Paper number 93JC00651.
0148-0227/93/93JC-00651$05.00

with those including the effects of various types of horizontally homogeneous cloud or aerosol layers. Cloud detection using AVHRR data is not addressed. For a discussion of polar cloud detection see *Key and Barry* [1989], *Sakellariou et al.* [1992] and *Yamanouchi et al.* [1987] and references therein.

METHODOLOGY

Our overall approach is as follows. We first simulate top-of-the-atmosphere (TOA) radiances for three thermal channels of the AVHRR instrument. Average clear-sky January conditions for the central Arctic are assumed. Operating in the NIR and IR "atmospheric window" regions of the spectrum, these channels are especially sensitive to surface emissions, but are also affected by any intervening atmospheric layer that absorbs/emits thermal radiation. Thus, surface (or skin) temperatures and emissivities are varied to evaluate the effects of different surface types. All modeled radiances are converted to equivalent blackbody temperatures (brightness temperatures) by inverting the Planck function [*National Oceanic and Atmospheric Administration*, 1991] to facilitate comparisons with physical temperatures and the analyses of bispectral results (NIR-IR brightness temperature differences) and derived thermal contrasts. Next, model clouds or haze layers are hypothetically inserted into the atmosphere to examine the behavior of simulated brightness temperatures and brightness temperature differences (BTD's) as a function of layer optical depth. These "split window" results are then examined for signatures that characterize haze, stratiform water clouds, clear-sky ice crystal precipitation (ICP) or high level cirrus clouds. Finally, by normalizing the difference between channel brightness temperatures of a lead pixel and its background (i.e. the multiyear ice pack) by the brightness temperature of the background scene normalized contrast values are derived and evaluated as a means to determine the limits of lead detection given certain sensor characteristics and atmospheric/surface properties.

Radiative Transfer Simulations

The radiative transfer code LOWTRAN 7 [*Kneizys et al.*, 1988] (hereafter simply LOWTRAN) is used to compute TOA, upwelling radiances from which satellite-derived brightness temperatures are simulated. LOWTRAN 7 is an extension and update of LOWTRAN 6 [*Kneizys et al.*, 1983] designed to compute atmospheric transmission or background radiance for prescribed spectral intervals ranging from 0.2 µm to infinity. Calculations are made for precribed viewing geometries accounting for atmospheric curvature. The code can be initialized for representative model atmospheres including intervening layers of cloud or haze, or for user-defined profiles of temperature, humidity and spectral extinction. An option to include multiple scattering effects is also available. The resolution of the model is 20 cm^{-1} at steps of 5 cm^{-1}. In cases involving haze, changes in the properties of aerosols as a function of relative humidity (RH) are accounted for [e.g., *Shettle and Fenn*, 1979; *Blanchet and List*, 1987] by first modifying the effective refractive indices of the bimodal particle size distribution and then recomputing extinction and absorption coefficients based on Mie theory [*Kneizys et al.*, 1980].

In this study we simulate AVHRR radiances for channels 3, 4 and 5. Channel 3 measures in the NIR window region of the spectrum and is centered at 3.7 µm while the IR channels 4 and 5 are centered at 10.8 µm and 12.0 µm, respectively. All our calculations include the effects of multiple scattered thermal radiation and are made at steps of 5 cm^{-1} (equivalent to 0.06 µm at 11 µm). The angular and spectral dependencies of snow and water emissivities are also taken into account. In all cases, LOWTRAN was initialized for average clear-sky January temperature and humidity profiles based on an analysis of Soviet ice island data collected in the central Arctic [e.g., *Key and Haefliger*, 1992; *Serreze et al.*, 1992]. The mean clear-sky January temperature and dewpoint temperature profiles are shown in Figure 1 with the boundaries of subsequently prescribed hypothetical layers of haze, stratus cloud, cirrus cloud and ice crystal precipitation indicated. Because there is essentially no information available on the vertical structure of atmospheric gases in the central Arctic, we assume that average "subarctic winter" concentrations of O_3, CH_4, CO and N_2O exist in the atmosphere when running LOWTRAN. Model subarctic winter background aerosol concentrations for the troposphere (2 to 10 km) and the stratosphere (10 to 30 km) were also prescribed. To simulate haze effects, boundary layer (0 to 2 km) aerosol concentrations were varied by specifying the layer visibility, but in all other cases the default "rural" aerosol model for the boundary layer was used. To examine the full range of AVHRR scan angles (0° to approximately 55°) we made calculations at 0° (nadir), 20° and 50°. Only results for 0° and/or 50° are presented here.

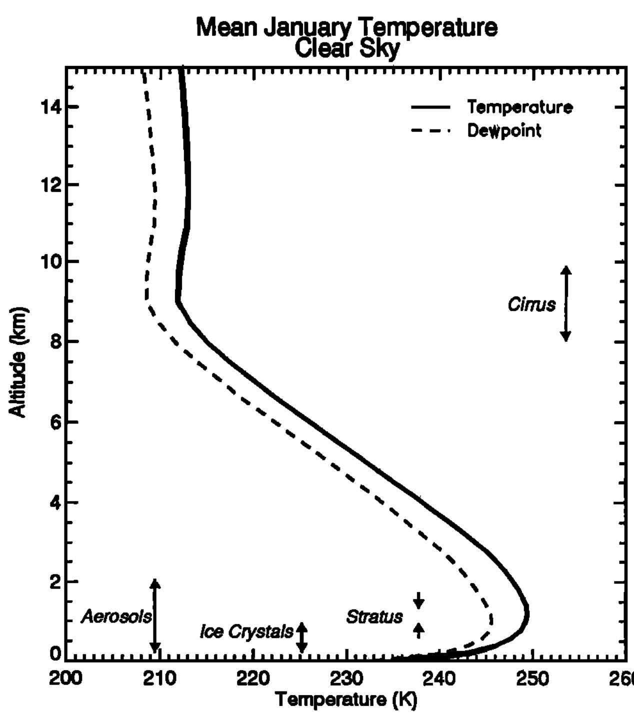

Fig. 1. Mean clear-sky January temperature and dewpoint temperature profiles for the central Arctic. Also shown are the vertical positions of hypothetical layers of cirrus cloud, boundary layer haze, ice crystal precipitation and stratus cloud that are prescribed for radiative transfer simulations that are described in the text.

Intervening Atmospheric Effects

The effects of four commonly observed atmospheric phenomena in the Arctic are considered: (1) Arctic haze [e.g., *Rahn and McCaffrey*, 1980; *Valero et al.*, 1989; *Valero et al.*, 1983] which persists over large regions of the Arctic, especially during late winter and early spring, (2) Arctic stratus cloud [e.g., *Tsay and Jayaweera*, 1984; *Tsay et al.*, 1989; *Curry et al.*, 1992] which commonly obscures satellite viewing of the sea ice surface in summer, but may be thin enough during the winter months to make lead detection feasible, (3) clear-sky ice crystal precipitation (ICP) which has a significant effect on the radiation balance of the surface/atmosphere system in the Arctic [*Curry et al.*, 1990; *Curry et al.*, 1989a; *Curry et al.*, 1989*b*], and (4) high level cirrus clouds which are the "most-frequently-occurring cloud type" observed in the central Arctic during winter and spring [*Warren et al.*, 1988]. Each of these has a distinct effect on the upwelling thermal radiation emitted from the underlying surface and atmosphere depending on their microphysical properties, geometric thicknesses and positions within the atmosphere. The differences in the radiative properties of atmospheric aerosols (haze), water droplets or ice crystals result in varying degrees of scattering and absorption as a function of wavelength. These differences can be exploited using multispectral techniques to distinguish various types of attenuating layers that may exist in the Arctic atmosphere assuming that the underlying surface properties can be determined by other means.

Upwelling radiation is also very sensitive to the temperature of any intervening layers which depends on the vertical position of those layers [*Stone*, 1993]. Layers having similar thickness and microphysical properties can affect satellite-derived brightness temperatures quite differently depending on their height because the atmosphere is not generally isothermal. It is therefore important to obtain ancillary information about the physical properties of the atmosphere, the surface and any intervening layers as a first step in developing an algorithm to detect and map leads. We recognize that this need is currently a limiting factor in producing unambiguous results, but various prototype methods to remotely measure properties of the atmosphere and surface in polar regions have already been developed and show promise. For example, several objective methods to distinguish clear from "cloudy" pixels in satellite imagery have been proposed. These are based on multispectral techniques combined with radiative transfer theory [e.g., *Key and Barry*, 1989; *Yamanouchi et al.*, 1987; *Wahiche et al.*, 1986]. Also, a method to retrieve ice surface temperatures (IST's) using AVHRR thermal imagery [*Key and Haefliger*, 1992] has been proposed, and improvements have recently been reported on the retrieval of temperature and humidity profiles over sea ice using data from the TIROS-N Operational Vertical Sounder (TOVS) as well [*Francis*, 1992]. Validation of these various algorithms has not been thorough, however. Process studies based on actual field measurements in conjunction with satellite image analysis are needed to confirm theoretical results. An analysis of in situ data collected in the vicinity of the Beaufort Sea during the 1992 spring Leads Experiment (LEADEX) combined with coincident satellite image analyses should provide a valuable opportunity to validate a variety of multispectral techniques proposed for operational use.

Arctic Haze. The optical properties of Arctic haze have not been extensively measured, but model calculations indicate that the volume extinction coefficients of Arctic hazes are to a first approximation the same order of magnitude as those for tropospheric aerosols [e.g. *Blanchet and List*, 1983; *Tsay et al.*, 1989]. Because Arctic haze generally contains an anthropogenic component of carbonaceous material transported from the lower latitudes [*Rosen et al.*, 1981; *Kahl and Hansen*, 1989], the "urban" aerosol model of LOWTRAN was selected to simulate low level haze layers. This model represents a mixture of 20% soot-like aerosols and 80% rural type aerosols contained in the 0 to 2 km boundary layer [*Kneizys et al.*, 1980]. The extinction coefficient β for boundary layer haze as defined in LOWTRAN is determined from a prescribed atmospheric visibility V using Koschmieder's formula: $V = 1/\beta \ln(1/\hat{\varepsilon})$, where $\hat{\varepsilon}$ is a threshold contrast taken to be 0.02.

The infrared opacity of aerosol layers is known to increase quite dramatically with increasing relative humidity [*Blanchet and List*, 1987; *Shettle and Fenn*, 1979], thus an assessment of how water uptake by hygroscopic aerosols affects simulations of brightness temperatures and BTD's was also made. Results for a saturated haze layer (RH = 99.9%) composed of "wet" aerosol particles are contrasted with those for moderately dry (RH ≈ 70%) haze layers found to characterize mean January conditions in the Arctic. LOWTRAN is designed to modify the absorption and scattering coefficients of aerosol distributions by (1) assuming growth of particulates as a function of RH based on the results of *Hanel* [1976], (2) adjusting their effective refractive indices, and (3) recomputing their radiative properties based on Mie theory [*Kneizys et al.*, 1980].

Arctic Stratus. Arctic cloud climatologies show marked increases in average low cloud amounts during spring attributed to the presence of stratiform water clouds within the boundary layer which reach a maximum coverage of about 70% during the summer months [*Huschke*, 1969; *Vowinckel and Orvig*, 1970]. Stratus clouds have a potentially dramatic impact on the surface-atmosphere heat budget depending on whether their shortwave albedo effects or longwave greenhouse effects dominate the lower tropospheric radiation balance [*Curry et al.*, 1992]. Summertime visible stratus optical depths tend to be large, in cases exceeding 20 [*Herman and Curry*, 1984]; thus the use of visible imagery to detect leads is not practical, and because thermal contrasts between leads and multiyear sea ice tend toward zero as cloud opacity increases, detection using thermal imagery is also impractical in most cases. During winter, however, stratus cloud cover is often less than 20% and the cloud layers tend to be thin optically with visible optical depths on the order of 2 [*Curry et al.*, 1992]. Detecting leads using thermal imagery in winter may, therefore, be possible. Using the LOWTRAN model for "stratus" we assess the feasibility of detecting leads during winter by assuming that a horizontally homogeneous cloud layer 380 m thick exists in the lower atmosphere as indicated in Figure 1. For stratus simulations the desired range of visible (0.55μm) optical depth τ was obtained by varying the conversion factor from equivalent LWC (g m^{-3}) to extinction coefficient (km^{-1}) in the LOWTRAN code [*Kneizys et al.*, 1988]. The stratus droplet size distribution is represented by a modified gamma distribution:

$$n(r) = 27r^2e^{-0.6r}$$

where r is the droplet radius and n is number density. The total number density is taken to be 250 cm^{-3} and the mode radius is 6.67μm (for mass distribution). Details of the LOWTRAN cloud models are given in *Shettle et al.* [1988].

Layers of Ice Crystals. Both the high level cirrus cloud and low level ice crystal precipitation simulations were made by inserting the LOWTRAN "standard" cirrus model [*Shettle et al.*, 1988] into the atmosphere at the vertical positions indicated in Figure 1. For both conditions the desired range of optical depth was obtained by assuming the appropriate values of 0.55μm volume extinction coefficients for a 2 km thick cirrus based at 8 km and a 1 km thick ICP layer based at the surface. Note that ice crystal precipitation has been observed from the surface to heights exceeding 3 km in the Arctic, but it is most frequently observed below about 1 km [*Curry et al.*, 1990].

For all of the cases discussed above theoretical calculations were made for a visible optical depth range of 0 (clear-sky) to 100, but results are presented only for values between 0 and 10. Realistic layer thicknesses and extinction values of aerosols and ice crystals are such that visible optical depths rarely exceed 10 and although stratus optical depths may exceed this value during the summer months, low thermal contrasts and high visible opacity preclude lead detection at this time of year. In the winter, even when mixed-phase layers contain small amounts of liquid water, optical depths are generally within the range represented here.

Surface Characteristics

Model runs were initialized for three different surface temperatures to characterize open or refrozen leads and a fourth temperature representing the surrounding ice pack which is assumed to be 2 m thick and in equilibrium with the surface air temperature. In the discussion that follows, the terms "skin" and "surface" temperature are used interchangeably and should not be confused with shelter temperature (measured 2 m above ground level) which is generally higher than the actual skin temperature when a surface-based temperature inversion exists. Shelter temperature may differ from skin temperature by more than 10°C depending on the region and time of year [e.g., *Stowe et al.*, 1988; *Rossow et al.*, 1989]. Because the surface types of interest here are nearly "black" (having emissivities approaching unity) in the AVHRR NIR and IR spectral bands, surface emissions dominate the upwelling radiation field under clear skies. And even when moderately opaque haze or cloud layers are present, surface emissions greatly influence TOA radiances, thus realistic specifications of skin temperatures are necessary to produce meaningful theoretical results. Similarly, to validate any lead detection algorithm based on bispectral differences and/or derived IR or NIR contrasts it will be essential to first implement an accurate surface temperature retrieval algorithm.

Because measurements of skin temperatures as a function of lead thickness have not been made in the central Arctic during winter, we estimate these temperatures using an energy balance model following the method of *Maykut* [1982]. The energy balance equation is

$$(1-\alpha)F_r - I_{ice} + F_L + \varepsilon\sigma T_{ice}^4 + F_s + F_e + F_c = 0$$

where α is the shortwave albedo of the surface, ε is the longwave emissivity of the surface, σ is the Stefan-Boltzmann constant, I_{ice} is the amount of shortwave energy transmitted through the ice, F_r and F_L are the downwelling shortwave and longwave radiative fluxes, respectively, F_s and F_e are the sensible and latent heat fluxes, respectively, and F_c is the conductive heat flux. A flux toward the surface is positive. The sensible and latent heat fluxes are primarily dependent on the wind speed, air temperature and the temperature of the ice T_{ice}.

The downward longwave fluxes were modeled using LOWTRAN, again assuming the mean clear-sky January temperature and humidity profiles. The shortwave component is zero for winter energy balance simulations. Realistic values of F_s, F_e and air temperature were prescribed in the energy balance equation based on concurrent meteorological data collected on the ice island. Following this procedure three temperatures were computed to represent a range of lead types: for open leads, 271 K; for leads covered by 5 cm thick ice, 256 K; and for 15 cm thick leads, 248 K. The ice pack was assumed to be in thermal equilibrium with the surface air and was assigned a temperature of 235 K, the mean temperature computed from measurements made at the first rawinsonde level during January.

All surfaces with the exception of open leads are assumed to be snow-covered and directional snow emissivities were modeled following the procedure in *Dozier and Warren* [1982]. This method involves calculating the single scattering albedo, asymmetry factor and phase function for snow grains using a Mie code before determining the directional, wavelength-dependent emissivities using the delta-Eddington approximation of the radiative transfer equation. These emissivities were then integrated over the response function for each channel i:

$$\varepsilon_i(\theta) = \frac{\int_{\lambda_1}^{\lambda_2} \varepsilon(\lambda,\theta)\phi_i(\lambda)\, d\lambda}{\int_{\lambda_1}^{\lambda_2} \phi_i(\lambda)\, d\lambda}$$

where $\varepsilon(\lambda,\theta)$ is the emissivity in the direction θ at wavelength λ and ϕ_i is the ith sensor response function. *Key and Haefliger* [1992] note that differences between the integrated emissivities for the NOAA series 7, 9, and 11 AVHRR sensors are on the order of 0.0001. In the current study we use the NOAA 7 values only. For brightness temperature simulations over open leads, the angular dependence of channel emissivities of water are determined through Fresnel calculations. Table 1 gives the angular emissivities used in the current analysis as a function of AVHRR scan angle and surface type. In reality, newly refrozen leads are clear of snow; thus pure ice emissivities should be used for best results. However, the authors are aware of no comprehensive set of measurements nor method from which the spectral, directional emissivities of planar ice can be determined. The emissivity of ice approaches unity and is often assumed to be 1.0 for field investigations [e.g., *Konig-Langlo and Zachek*,

TABLE 1. Angular Emissivities of Snow and Water in NOAA 7 AVHRR Channels 3, 4 and 5 at Two Satellite Scan Angles

	Snow		Water	
Channel	0°	50°	0°	50°
3	0.998	0.992	0.976	0.961
4	0.999	0.996	0.992	0.984
5	0.996	0.987	0.986	0.972

1991]. A more accurate value may be 0.97 [*Hobbs*, 1974] which is within 2% of the snow values listed in Table 1. Thus, the assumption that all surfaces are snow-covered will not result in serious errors in simulated brightness temperatures nor will differences in channel brightness temperatures or contrast ratios be affected significantly.

For even more accurate simulations of brightness temperatures, channel radiances should also be integrated over the appropriate sensor response functions. These vary from one satellite to another as discussed in *Key and Haefliger* [1992]. In that study, they found that by using the full response functions instead of assuming rectangular functions (i.e., 100% response at all wavelengths within the portion of the channel where the actual response is at least 50%) the brightness temperature differences were only on the order of 0.05 K for channel 4, but were about 0.5 K for channel 5 assuming typical January conditions in the central Arctic. Because we focus here on channel 4 results, we use the rectangular function for all simulations rather than performing this time-consuming integration. This is justified in that the computation of normalized contrasts are based on differences and ratios of brightness temperatures at one or another wavelength so that small absolute biases due to differences in response functions have a negligible effect on the final results.

RESULTS

Simulated Brightness Temperatures

Examples of channel brightness temperatures as a function of visible (0.55 µm) optical depth are shown in Figure 2 for boundary layer haze, ice crystal precipitation and high-level cirrus clouds at 0° and 50° satellite scan angles for channels 3, 4, and 5 of the AVHRR instrument. These layers were positioned as shown in Figure 1 and mean January temperature and humidity profiles were assumed. Within each panel (from top to bottom) are plots that relate to the different prescribed surface temperatures representing open leads, leads of 5 cm and 15 cm thickness (271 K, 256 K and 248 K, respectively), and the multiyear pack ice (235 K). Note that the boundary layer is moderately dry during January in the central Arctic with RH averaging about 70% between the surface and 2 km suggesting a predominance of clear skies containing low concentrations of dry aerosols during this time of the year. At zero optical depth the physical surface temperatures are reasonably well represented by simulated channel brightness temperatures because the selected channels are all within NIR and IR window regions of the spectrum where sensitivity to the relatively dry Arctic atmosphere is least and because open water, newly refrozen leads and snow-covered surfaces all have high emissivities. Regardless of the underlying surface type, channel 3, 4 and 5 brightness temperatures tend to converge to the blackbody radiating temperature of the top of the intervening cloud or haze layers as optical depths increase, though the rate of convergence varies depending on the microphysical properties of the intervening layer and the layer's position and mean temperature relative to the surface. Scan angle effects are also apparent by comparing corresponding panels for 0° and 50° viewing angles. No matter what type of surface or intervening medium exists, the convergence of simulated brightness temperatures to layer top temperatures occurs faster when viewing off-nadir. This is due to the increase in optical path length by a factor $1/\cos(\theta)$, where θ is the satellite scan angle as viewing angles increase from nadir.

Because haze particles absorb and emit much less NIR and IR radiation than do ice particles or water droplets at a given visible optical depth, haze layers neither attenuate nor enhance significantly the thermal emissions from the surface. Thus, simulated NIR and IR brightness temperatures during typical winter conditions are not very sensitive to changes in aerosol loading in the boundary layer. In these situations, the relatively dry haze layers become essentially black at visible optical depths exceeding 95 (equivalent to an infrared optical depth of about 6). This extreme value corresponds to an unrealistic visibility of less than 85 m. As noted by *Blanchet and List* [1987], however, the infrared opacity of aerosols increases dramatically as relative humidity increases. In fact, IR optical depths may exceed those for visible wavelengths in saturated haze layers. This phenomenon occurs due to the uptake of available water by hygroscopic particles such as sulfuric acid and deliquescent compounds within the layer causing a shift to a larger particle size distribution and corresponding enhancements of the absorption and scattering cross sections of the particles.

We evaluated the effects of increasing relative humidity on aerosol layers by hypothetically saturating the 0 to 2 km layer and recalculating the brightness temperatures for a "wet" aerosol layer. This is easily accomplished using LOWTRAN because the absorption and scattering coefficients are modified in accordance with hygroscopic growth as described previously. The optical depth dependence of channel 4 brightness temperatures for a haze layer with mean RH = 99.9% was found to be virtually identical to that for a haze layer having RH = 70% while channel 5 brightness temperatures tended to converge slightly faster to the blackbody temperature of the layer. The NIR channel 3 simulations revealed the most pronounced change due to saturation. They indicated slightly faster convergence with increasing optical depth than either of the IR channels and also, interestingly, NIR values converge to a temperature below the physical temperature of the layer top. This leads to negative NIR-IR spectral differences. Qualitatively, an optically thick, saturated haze layer has similar radiative behavior as does a stratiform water cloud. As these layers increase in opacity they become black to infrared radiation resulting in a rapid convergence of brightness temperatures (no matter what the underlying surface is) to the physical

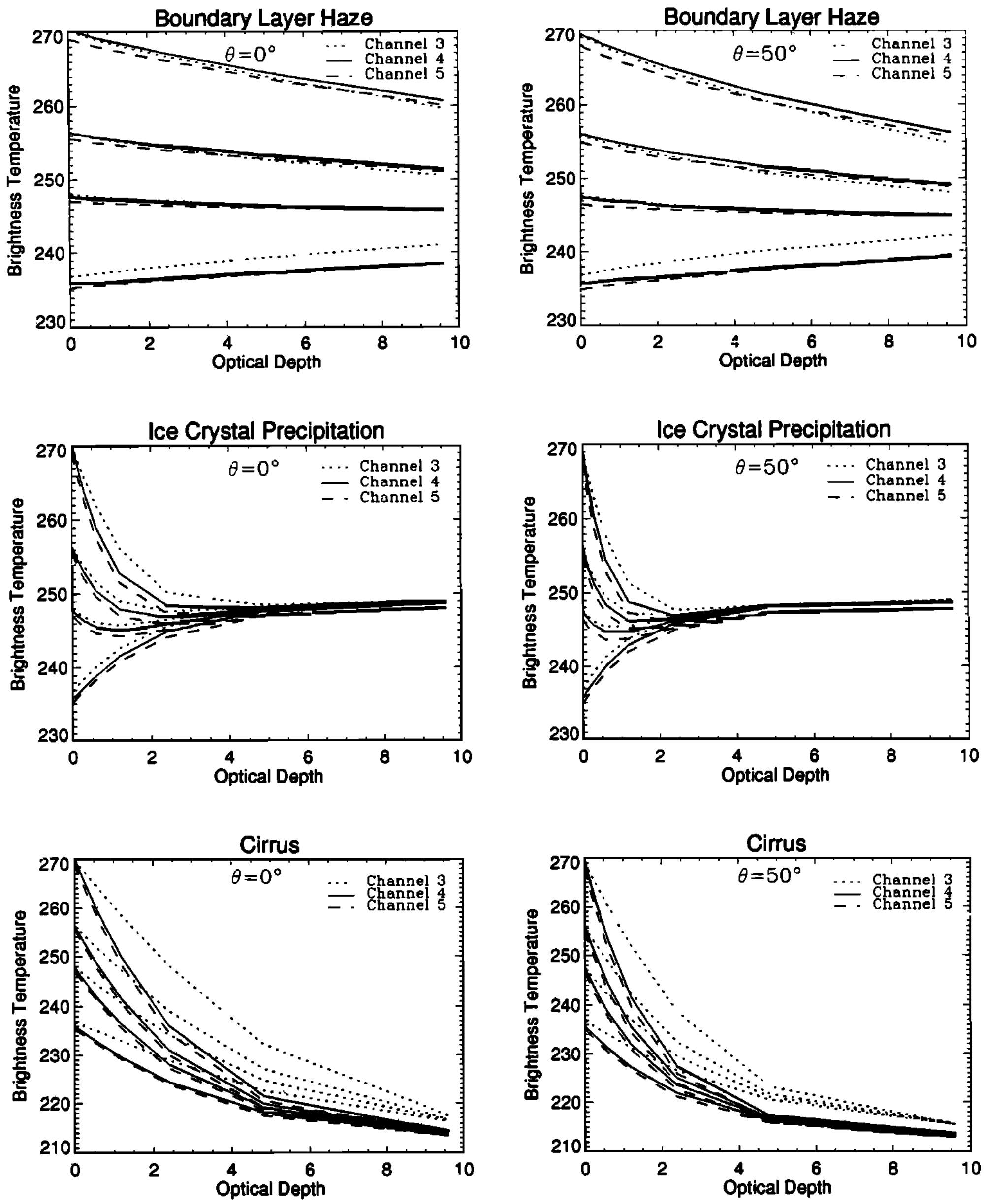

Fig. 2. Simulated brightness temperatures for layers of boundary layer haze, ice crystal precipitation and high-level cirrus cloud for three AVHRR thermal channels assuming four surface types (from top to bottom at left of each panel): open water, 5, 15, and 200 cm thick ice. Results are shown for satellite view angles of 0° and 50° over a range of 0.55 µm optical depths between 0 and 10. Mean clear-sky January temperature and humidity profiles for the central Arctic are assumed.

temperature of the layer top; but in the NIR, thick layers totally attenuate the upwelling radiation from the surface while contributing little to TOA radiances because these layers have low NIR emissivities. Thus, NIR brightness temperatures are actually colder than corresponding IR values [e.g., *Yamanouchi et al.*, 1987]. These are important considerations because the relative magnitudes of NIR-IR bispectral differences as a function of relative humidity, phase and optical depth may be exploited to distinguish different types of intervening atmospheric layers.

The importance of knowing the vertical position of an intervening layer is apparent by comparing the results for the low level ICP with those for high cirrus clouds. Both layers have identical microphysical and radiative properties based on the standard LOWTRAN cirrus model. However, their net radiative effect on the upwelling radiation field differs significantly because of their relative temperatures and proximity to the nearly black underlying surfaces. Brightness temperatures above the ICP layer converge more rapidly with increasing optical depth than do corresponding temperatures above cirrus because the top of the ICP layer coincides with the warmest region of the atmosphere which is directly influenced by surface emissions. Radiation emitted by the surface contributes significantly to the total upwelling radiation through absorption and secondary emission by the ICP layer at a relatively warm layer temperature. A similar radiative effect occurs in the case of cirrus, but the cold, dry atmosphere below the cirrus layer has little effect on the upward radiative flux and the cloud particles themselves absorb and re-emit this radiation at a much colder temperature. As with haze and stratiform water clouds, these different radiative effects give rise to distinct signatures of brightness temperatures and bispectral differences as a function of optical depth.

NIR-IR Bispectral Differences

Differences in BTD signatures for combinations of surface and layer types as a function of optical depth may be used to distinguish varying surface and atmospheric properties within a satellite scene, a necessary step in developing a lead detection algorithm. For example, at a cirrus optical depth of about 3.0 the BTD between channel 3 and channel 4 (T_{b3} - T_{b4}) over an open lead is approximately 13 K whereas this difference is only about 2 K if a low level ICP layer of equal optical depth is present as viewed at nadir.

To more clearly illustrate the potential use of split window imagery to distinguish between various cloud and aerosol layers that are common in the Arctic, Figure 3 was constructed. Shown are values of (T_{b3} - T_{b4}) for three different layers already discussed, dry (70% RH) and wet (99.9% RH) haze layers within the boundary layer and ICP in the lowest kilometer of the atmosphere, and in addition, results are given for the stratus layer described above and shown in Figure 1. Each panel includes plots of the simulated T_{b3} - T_{b4} values for the four surface types assuming a scan angle of 0°. It is clear that bispectral differences are sensitive not only to optical depth but also to relative humidity and the phase of the particles. Bispectral signatures for dry aerosols are insensitive to increasing optical depth except for those related to multiyear ice. Under saturated hazy conditions there is a distinct monotonic decline in BTDs with increasing τ over all surface types with negative values observed except over multiyear ice when $\tau \leq 5$. Such separations between multiyear ice signatures and other surface types should permit better identification of background pixels needed to normalize thermal contrasts for the purpose of distinguishing leads (details are given in the following section). If a stratus layer is present within the warm region of the atmosphere a sharp fall-off to significantly large negative values occurs in the range of optical depths between 0 and

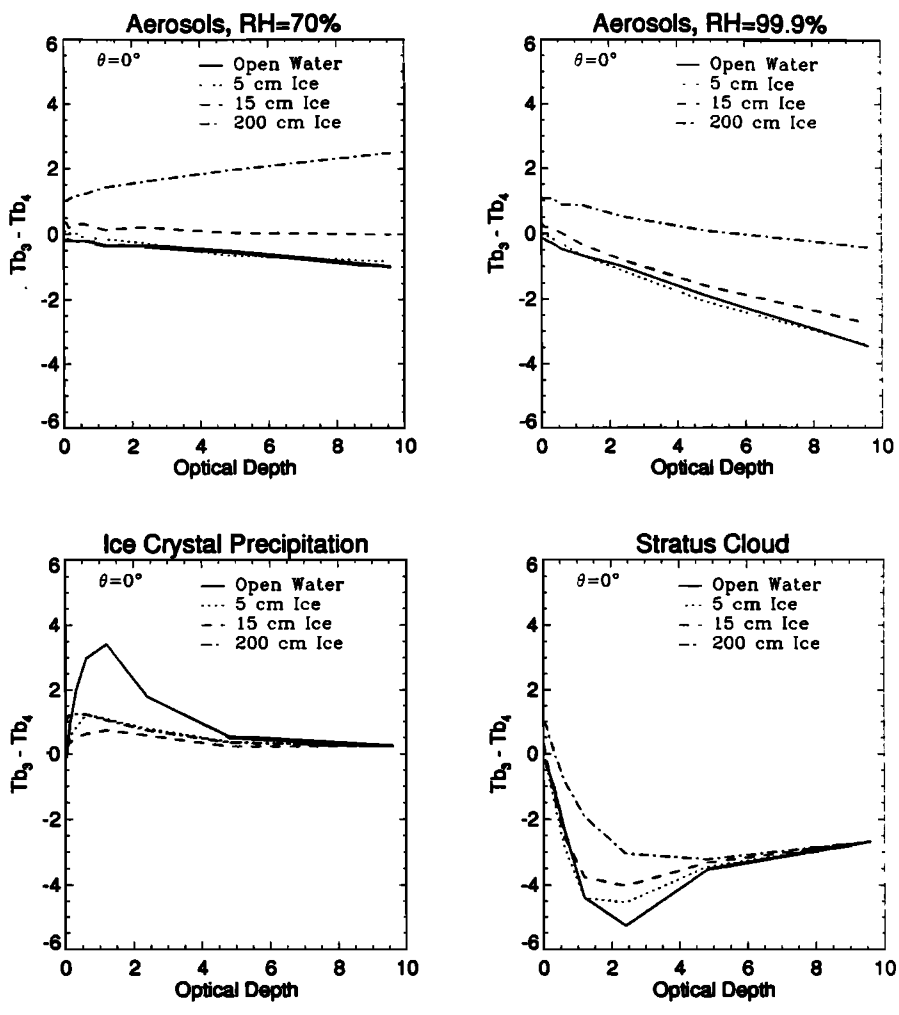

Fig. 3. AVHRR channel 3 minus channel 4 brightness temperatures as a function of 0.55 µm optical depth for four intervening layer types: aerosol layers having mean relative humidities of 70% and 99.9%, respectively, ice crystal precipitation and stratus cloud. Brightness temperature differences are shown for the four surface types described in the text.

about 2.5 with a converging upward signal as τ increases further. In the case of a low-lying ICP layer, positive differences of 0.5 K to 3.5 K peaking between optical depths of 0.5 and 1.5, are apparent, whereas for a similar (cirrus) layer placed high in the atmosphere BTD's as large as 13 K were noted for $\tau \approx 2.5$ (see Figure 2). In theory, if TOA NIR and IR radiances can be measured accurately, much information can be extracted by analyzing bispectral images. Unfortunately, the AVHRR channel 3 data is reported to be too noisy to be useful for cloud detection at cold temperatures [*Yamanouchi et al.*, 1987], but hopefully, future spaceborne radiometers will provide data of sufficient quality to resolve the signatures described here.

One of the primary advantages of using a split window technique is its applicability to daytime or nighttime images. Though not the focus of the current study, LOWTRAN was also used in a radiance mode including the effects of single scattered solar radiation to make a preliminary evaluation of the effect that NIR reflections from the surface and/or aerosol layers have on NIR-IR differences. Dramatic differences between day and night simulations were found due to the additional contributions of reflected solar NIR radiation during the day while the infrared fluxes remained unchanged. This effect has also been noted for high level cirrus clouds [*Stone et al.*, 1990; *Stephens*, 1981]. Figure 4 exemplifies how NIR reflections affect T_{b3} - T_{b4} signatures when single scattered solar radiation is included in the model calculations. The lower composite of curves are the T_{b3} - T_{b4} values shown previously in Figure 3 for an aerosol layer having a mean relative humidity of 70%. The upper set of curves (bold lines) shows the behavior of T_{b3} - T_{b4} for an identical haze layer and surface conditions, but includes the reflected solar radiation component when the sun is arbitrarily placed at a zenith angle of 75° and an azimuth angle of 30° relative to a satellite viewing at 50° off nadir. Daytime brightness temperature differences are significant even at zero optical depth and increase with τ regardless of surface type. For extreme aerosol optical depths (not shown), T_{b3} - T_{b4} approaches a constant value as the diffuse limit of NIR reflection is reached and the layer begins to emit as a blackbody in the infrared. Qualitatively, similar positive enhancements in NIR-IR brightness temperature differences are expected for water clouds when the sun is above the horizon. Also, the dramatic contrast between low clouds and snow-covered surfaces in the NIR during sunlit periods makes the analysis of AVHRR channel 3 imagery a potentially powerful tool for discriminating clouds over snow [*Kidder and Wu*, 1984].

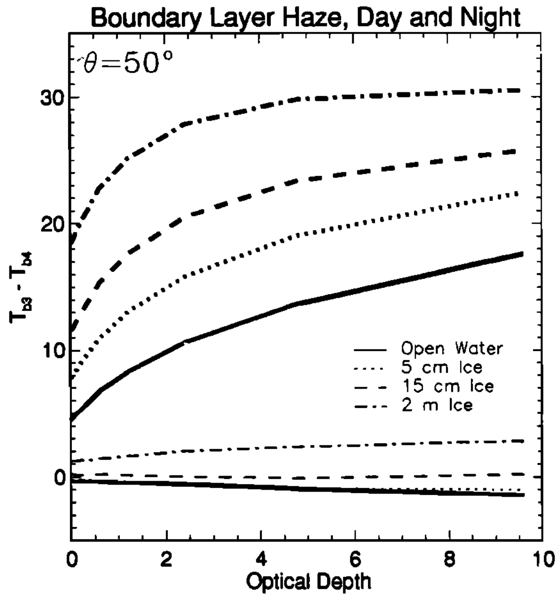

Fig. 4. Differences between AVHRR channels 3 and 4 brightness temperatures as a function of boundary layer haze optical depth at 0.55 µm during the day (thick lines) and at night (thin lines) over each of the four surface types described in the text. Satellite scan angle is 50°, solar zenith angle is 75° and solar azimuth angle is 30°.

Normalized Atmospheric Contrast

Normalized atmospheric contrast is a wavelength dependent quantity, varying with atmospheric opacity, expressed in terms of the brightness temperature difference between any given pixel and the background scene normalized by the brightness temperature of the background (in this case taken to be the 2 m thick multiyear ice):

$$C(\tau,\lambda) = \frac{T_T(\tau,\lambda) - T_B(\tau,\lambda)}{T_B(\tau,\lambda)} \qquad (1)$$

where T_T is the brightness temperature of the target (lead) and T_B is the background brightness temperature. Hereafter, in all expressions involving contrast the wavelength dependence is assumed and the λ is omitted. Figure 5 shows the behavior of this quantity for IR channel 4 derived from the results presented in Figure 2. This measure of contrast provides a potentially powerful means to detect leads using thermal imagery both for daytime and nighttime conditions. Although, in most cases, Figure 4 indicates a rapid decrease in normalized contrasts as optical depth increases, realistic cirrus, ICP or haze optical depths are generally within a range that should permit the resolution of leads using thermal contrasts provided that radiances can be measured accurately, sensor field-of-view is small relative to lead widths and full use of ancillary data is made. *Curry et al.* [1990] for instance, measured ICP visible optical depths ranging from about 0.03 to 20, but in five out of seven cases, τ was less than about 5, within a range in which thermal contrast should be measurable. With regard to cirrus, even for large extinction coefficients their optical depths are limited because they are confined to regions of the upper troposphere bounded above by the tropopause. As an example, a cirrus cloud having a large visible volume extinction coefficients, say κ_{ext} = 0.2 km^{-1}, 7 km thick (ΔZ = 7.0) would have an optical depth of only 1.4, where $\tau = \kappa_{ext}\Delta Z$. Such large extinctions would exist only for cirrus composed of very large ice crystals with proportionally large total ice water contents (IWC's) [e.g., *Stone et al.*, 1990] which occur rarely in extremely cold environments [e.g., *Stone*, 1993; *Platt and Harshvardhan*, 1988; *Heymsfield and Platt*, 1984]. In cases involving haze, the aerosol loading would need to be extreme before thermal contrasts diminished significantly. There is no observational evidence that aerosol layers can attain optical

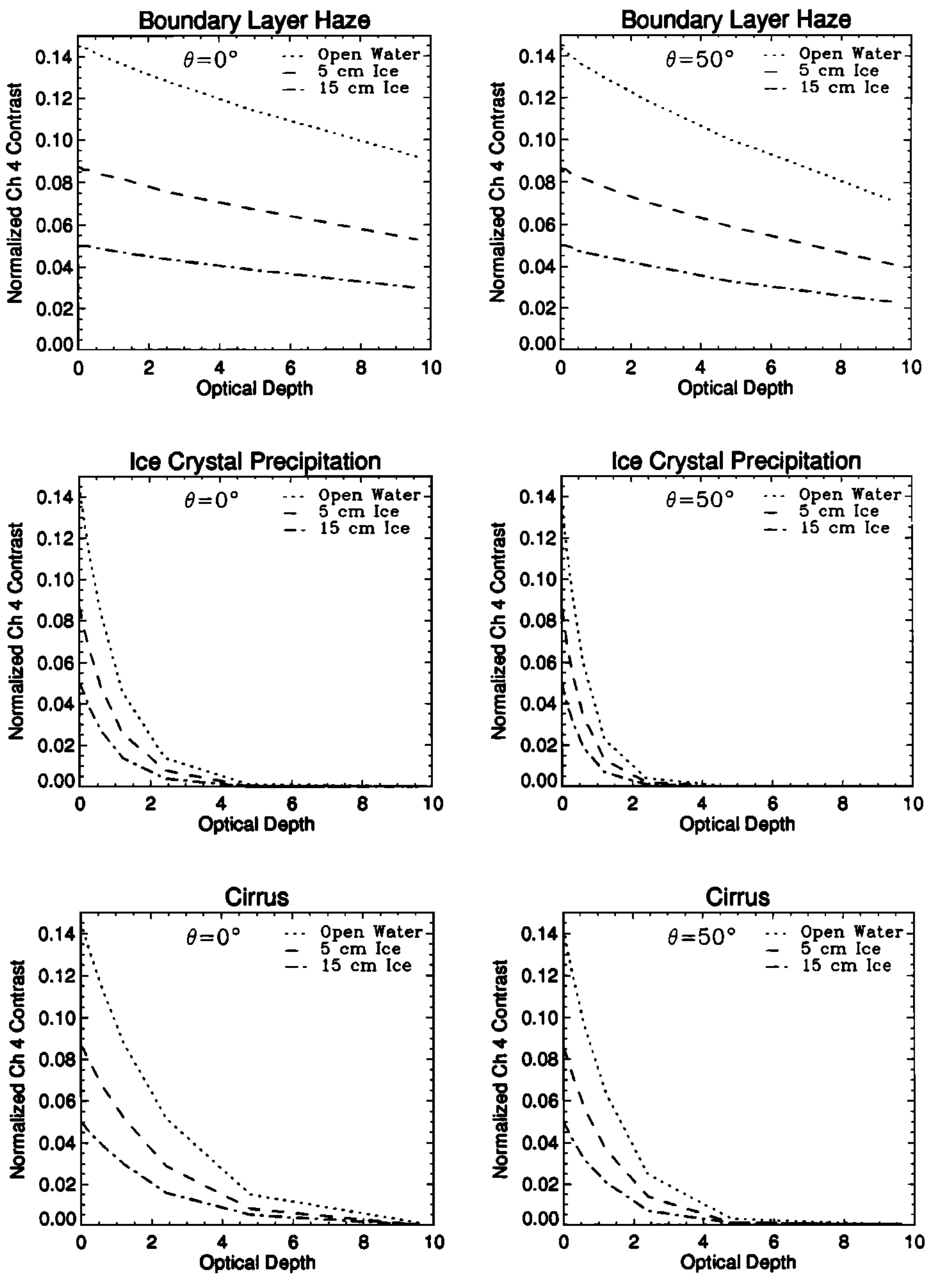

Fig. 5. Normalized AVHRR channel 4 contrasts between three lead ice thicknesses (open water, 5 cm and 15 cm ice) and the background 2 m thick ice for boundary layer haze, ice crystal precipitation and high-level cirrus cloud as a function of 0.55 μm optical depth. Results are shown for satellite view angles of 0° and 50° derived from the brightness temperatures shown in Figure 2.

depths that would preclude lead detection using thermal imagery. For instance, mean 0.5 μm optical depths for haze layers observed over Barrow, Alaska, even when nearly saturated, were only about 0.2 [*Mendonca et al.*, 1981] and the maximum 0.5 μm optical depth measured during what has been described as a "megahaze" event was about 0.7 [*Dutton et al.*, 1989]. Of course, mixed phase haze layers containing large concentrations of ice crystals will tend to attenuate thermal radiation much like pure ICP layers do.

Finally, channel contrasts for the 380 m thick stratus cloud (computed but not shown) were also analyzed to evaluate whether or not leads are detectable during winter when stratus layers tend to be optically thin. IR channel brightness temperatures for the four surface types were observed to converge in a similar manner as was noted for the boundary layer ICP (Figure 2); thus simulated IR contrasts under the influence of stratus clouds are nearly equal to those computed for the ice crystal precipitation layer shown in Figure 5. The convergence of channel 3 brightness temperatures with optical depth was found to be even more rapid than for the IR channels so that NIR contrast values diminish more quickly with optical depth. Both IR and NIR contrasts are likely to be below measurable threshold values (discussed below) to make lead detection possible when stratus layers are present because their optical depths are typically in the range of 2 or greater. Our simulations indicate that normalized contrasts will be very difficult to resolve at this level of opacity.

Lead Detection Based on Critical Contrast

The normalized contrast $C(\tau,\lambda)$ in (1) is defined in terms of the target (lead) and background (multiyear ice) temperatures but says nothing about the geometrical characteristics of the target or imaging system. In such a context it assumes that a given lead pixel is completely within the FOV of the satellite radiometer. We now examine how contrast varies as a function of lead width and sensor field-of-view to account for image pixels that contain both lead and multiyear ice surface types.

Letting p be the fractional area covered by a lead within a pixel; i.e., p = width/FOV, the total contrast C_{tot} that takes into account the reduction in temperature contrast due to atmospheric and spatial effects is

$$C_{tot}(\tau) = \frac{[pT_T(\tau)+(1-p)T_B(\tau)]-T_B(\tau)}{T_B(\tau)}$$
$$= pC(\tau)$$

If every pixel in the image is to be labeled as either a lead pixel or a background pixel, then some thresholding operation must be used. One possible method is to choose as a threshold the mean background temperature plus some multiple of its variability σ, say $T_B(\tau)+2\sigma$. (In reality σ may also be a function of τ.) As in (1), this threshold can also be expressed as a normalized (nondimensional) contrast ratio:

$$\gamma = \frac{2\sigma}{T_B(\tau)}$$

If the observed total contrast of a pixel is less than this value, then the pixel is considered part of the background scene. This threshold contrast includes implicitly the effect of the fractional area covered by a lead within a pixel; i.e., it is a total contrast. Low values of γ will generally result in more pixels being labelled as lead pixels because the background is more homogeneous when σ is small and thermal features should be more distinguishable. γ can also be defined in terms of some critical normalized atmospheric contrast:

$$C^*(\tau,\gamma) = \frac{\gamma}{p}$$

where the asterisk represents a threshold value. This expresses the normalized atmospheric contrast necessary for a lead to be detected if an intervening layer of optical depth τ is present.

To address the question of what minimum lead width can actually be resolved under specified atmospheric conditions and varying sensor FOV, we need to eliminate hypothetically the atmospheric effects. We therefore define the critical contrast of a lead as the normalized atmospheric contrast at zero optical depth $C^*(\tau=0,\gamma)$. We can relate $C^*(\tau,\gamma)$ back to the critical contrast $C^*(\tau=0,\gamma)$ with the data provided in Figure 5 which was used to construct Figure 6.

Figure 6 shows critical normalized contrast contours for leads as a function of p and optical depth for layers of aerosols, ICP and cirrus cloud assuming two values of γ. Note that the optical depth scales for ICP and cirrus have been decreased relative to the previous figures. As mentioned above, it is unlikely that contrasts in the presence of stratus would be sufficiently large at realistic values of stratus optical depth to permit lead detection, therefore stratus is omitted from this analysis. The contours in Figure 6 indicate the critical contrast that a pixel must exceed in order to be designated as a lead pixel once the threshold contrast γ is determined assuming mean clear-sky January conditions in the central Arctic. Such plots can be used to estimate the minimum lead width resolvable in an AVHRR channel 4 image under certain conditions as follows. Assume, for example, that the sensor's resolution is 1.0 km (FOV = 1.0) at nadir and a 1 km thick ICP layer is present above the surface. If we prescribe a normalized contrast threshold of 0.04 and a critical contrast of 0.10 as detection criteria, then Figure 6 can be used to estimate the narrowest resolvable lead as a function of the layer's optical depth. For an optical depth of 0.6, say, the width/FOV ratio is about 0.75, thus the narrowest detectable lead would be approximately 0.75 km wide. Under these conditions, any lead less than about 750 m wide would not be detectable if the ICP optical depth exceeded 0.6. Following the same approach but assuming an ICP optical depth of 0.3 now, the minimum detectable lead width is about 0.56 km if the same threshold criteria are used. If we relax the threshold criteria and do the same analysis for $\gamma = 0.02$, then a lead would need to be only about 400 m wide in order to be resolved at a pixel resolution of 1 km if $\tau = 0.6$, or about 290 m wide if $\tau = 0.3$. Note that for any given combination of optical depth, contrast threshold and critical contrast Figure 6 indicates that the minimum detectable lead width will be systematically smaller if, instead of ICP, either an aerosol layer or a cirrus cloud of equal optical depth is present.

It is suggested here that bispectral techniques be used in conjunction with image contrast analyses to develop an operational procedure to detect and map leads in the polar regions. However, because a continuum of signatures exist depending on atmospheric, surface and geometric effects, it will be essential to constrain the problem by first determining the state of the atmosphere and surface using a combination of multispectral techniques. Of particular importance will be the retrieval of surface temperatures [e.g., *Key and Haefliger*, 1992] because the thermal contrast between leads and the background ice pack depends critically on differences in surface emissions that determine the threshold of lead detection under varying atmospheric conditions.

DISCUSSION

The theoretical results presented above are enlightening, but we have obviously oversimplified the problems associated with lead detection. We have presented results that only represent average January conditions in the central Arctic and consider only four discrete surface types and four idealized hypothetical models to simulate what in nature is a complicated mix of intervening atmospheric effects. In reality, any of these variables assume a continuum of values that change spatially and temporally. Clouds and aerosol layers are naturally inhomogeneous having physical, radiative and microphysical properties that vary in space and time and frequently occur as

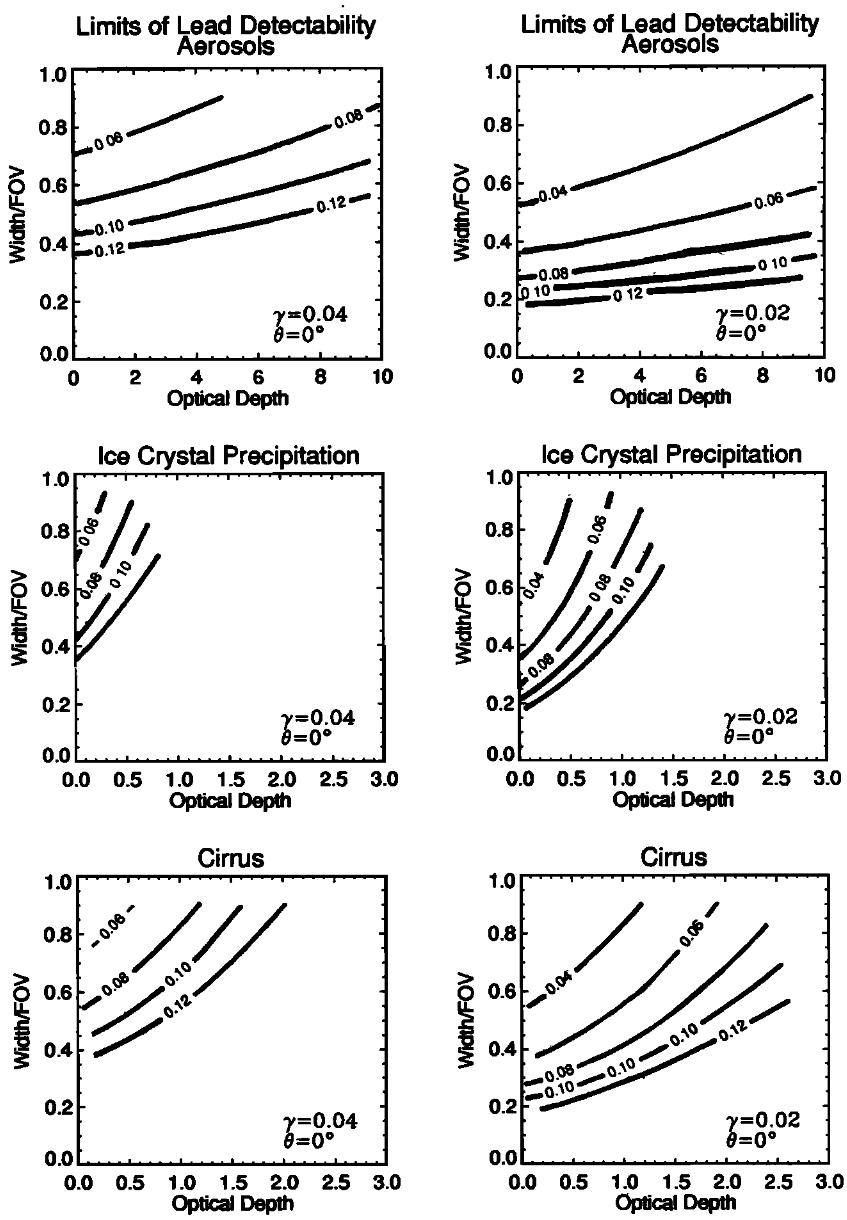

Fig. 6. Critical contrast of a lead as a function of its fractional coverage within an image pixel (width/FOV) and the 0.55 μm optical depth of aerosols (haze), ice crystal precipitation and cirrus cloud. For a given set of geometrical and atmospheric conditions the contours indicate the minimum contrast (at an optical depth of zero) that must exist in order for a lead to be detectable for specified values of threshold contrast γ assuming a satellite viewing angle of 0°. Mean clear-sky January conditions for the central Arctic are assumed. Results are given for two values of threshold contrast: γ=0.04 and γ=0.02 as defined in the text.

multiple layers of mixed phase particles. Intense winds, for example, dynamically force stratiform layers sometimes creating banded structures, especially for layers composed of condensed particles downwind of leads. The detection of leads is further complicated by constantly changing viewing geometries related to sensor FOV, satellite scan angle (and sun angle if daytime conditions exist). Nonlinear radiative effects are caused by increasing optical paths at the same time that pixel resolution degrades with increasing scan angle. To develop an operational lead detection algorithm, highly parameterized models will need to be used, perhaps in conjunction with comprehensive "look-up" tables listing expected contrast values and corresponding BTD's for a realistic range of combined surface and atmospheric properties. Furthermore, a step-wise approach will be necessary utilizing ancillary information to further constrain the problem. The use of cloud clearing algorithms is essential to assure accurate surface temperature retrievals and remote sounding techniques need to be improved in order to resolve atmospheric temperature and humidity profiles and to determine the physical, radiative and microphysical properties of intervening layers. Theoretically, multispectral analyses provide a basis for estimating these properties, but in reality it may be years before prototype methods are validated and approved for operational use.

Finally, comparisons between actual measurements and theoretical simulations are essential as algorithm development moves from a conceptual phase towards implementation. The data collected over the Beaufort Sea during LEADEX will hopefully provide case-by-case opportunities to verify the kinds of theoretical results presented in this paper and to further assess the feasibility of operational lead detection.

SUMMARY AND CONCLUSIONS

The use of the thermal channels of the AVHRR for the potential detection and mapping of leads has been evaluated for varying hypothetical atmospheric conditions and lead types. The detectability of leads is primarily dependent on the degree of thermal contrast between leads of different temperatures (thicknesses) compared to the background multiyear ice. Contrast varies with surface and atmospheric conditions and is a function of sensor characteristics including spectral response, FOV and viewing geometry.

The transfer of radiation through the atmosphere was modeled using LOWTRAN 7 initialized for mean clear-sky January temperature and humidity profiles computed from ice island data collected in the central Arctic and climatological values of atmospheric gas concentrations and background aerosols. Simulations of TOA radiances, expressed as brightness temperatures, were made for three channels of the AVHRR instrument. These calculations were made for a range of surface (skin) temperatures to simulate different lead types. The radiative effects of four atmospheric phenomena commonly observed in the Arctic were also estimated using models to simulate boundary layer haze, stratiform water clouds, ice crystal precipitation at low levels and high level cirrus clouds. View angle effects were assessed by prescribing a range of satellite scan angles. A preliminary evaluation of how increasing relative humidity affects thermal attenuation and emission by aerosol layers as related to lead detection was made. In addition, the radiative effects of reflected (solar) NIR radiation from aerosol layers was assessed. All calculations were presented for a visible optical depth range between 0 and 10 to facilitate comparisons of channel brightness temperatures, bispectral differences and derived values of thermal contrast. Results indicate that distinct signatures exist in the behavior of these quantities as a function of the intervening layers' optical depths depending on the microphysical and physical properties of the layers and their underlying surfaces.

Simulated brightness temperatures over haze were found to be least sensitive to increases in layer optical depth and showed small, essentially constant differences for NIR-IR channel pairs at night, but daytime simulations indicated significant enhancements in the NIR channel brightness temperatures due to solar reflections which lead to large brightness temperature differences. Because thermal extinction is minimal for haze layers and brightness temperatures vary little as a function of optical depth, normalized contrasts should be large enough to permit lead detection even under extremely turbid or saturated conditions unless haze layers include high concentrations of ice crystals.

Ice crystals in the atmosphere, either in the form of low-lying ice crystal precipitation or in the form of high level cirrus clouds, cause more significant perturbations to the upwelling radiation field. Simulated brightness temperatures for these layers tend to converge to blackbody values as optical depths increase thus reducing the contrast between surface types. Optically thick ICP layers potentially limit the use of thermal contrasts to detect leads. Based on limited observational evidence, however, ICP optical depths are generally small enough to permit contrast resolution in most cases if upwelling TOA radiances can be measured accurately.

Our theoretical results indicate that, if stratiform water clouds are present in the Arctic atmosphere, leads will not generally be detectable. Stratus clouds were found to have IR spectral signatures very similar to those for ICP as a function of optical depth, but are normally much more opaque due to their liquid water content. During summer stratus clouds obscure any view of the surface from space and even during winter when they contain only small amounts of liquid water, thermal contrasts are likely to be below reasonable thresholds of detection.

Through comparative analyses we find that bispectral signatures (NIR minus IR brightness temperatures) for various layer and surface types as a function of optical depth provide potentially useful information for minimizing ambiguous interpretation of thermal images. We suggest that the recognition of distinct multispectral signatures in conjunction with other remotely sensed properties of the surface and atmosphere may be a key step to developing an operational lead detection algorithm.

Finally, the concept of critical contrast was introduced whereby the sensor's field-of-view is quantitatively accounted for in order to estimate the width of the narrowest resolvable lead as a function of pixel FOV under varying atmospheric and surface conditions. Examples were given to demonstrate how the implementation of a thresholding technique may facilitate the development of an operational procedure for detecting and mapping Arctic leads. At present, however, the use of such a technique is limited due to our inability to remotely measure the properties of the Arctic atmosphere and surface accurately. Additional theoretical studies and validations using actual in situ and remotely sensed data are required as a critical step in the development of any specific lead detection algorithm. It is hoped that the data collected during LEADEX will provide the opportunity to verify the theoretical results presented in this paper.

Acknowledgments. This work was supported by ONR grant N00014-90-J-1840 and NASA grant NAGW-2407 (University of Washington subcontract 721566). Thanks are due to M. Serreze and J. Kahl for providing the Soviet ice island rawinsonde data (NA85RAH05066). We are also grateful to J. Curry for her useful comments and suggestions for improving this manuscript.

REFERENCES

Andreas, E.L., C.A. Paulson, R.M. Williams, R.W. Lindsay, and J.A. Businger, The turbulent heat flux from Arctic leads, *Boundary Layer Meteorol., 17,* 57-91, 1979.

Blanchet, J., and R. List, Estimation of optical properties of arctic haze using a numerical model, *Atmos. Ocean, 21,* 444-465, 1983.

Blanchet, J., and R. List, On radiative effects of anthropogenic aerosol components in Arctic haze and snow, *Tellus, 39B,* 293-317, 1987.

Curry, J.A., F.G. Meyer, and E.E. Ebert, Cloudless ice crystal precipitation in the polar regions, in *IRS'88 Current Problems in Atmospheric Radiation*, edited by J. Lenoble and J.F. Creleyn, pp. 80-83, A. Deepak, Hampton, Va., 1989*a*.

Curry, J.A., L.F. Radke, C.A. Brock, E.E. Ebert, Arctic ice-crystal haze, paper presented at AMS Symposium on the Role of Clouds in Atmospheric Chemistry and Global Climate, Am. Meteorol. Soc., Jan. 30 to Feb. 3, 1989, Anaheim, Calif., 1989*b*.

Curry, J.A., F.G. Meyer, L.F. Radke, C.A. Brock, and E.E. Ebert, Occurrence and characteristics of lower tropospheric ice crystal in the Arctic, *Int. J. Climatol.*, *10*, 749-764, 1990.

Curry, J.A., J. Schramm, and E.E. Ebert, Impact of clouds on the surface radiation balance of the Arctic Ocean, *Meteorol. Atmos. Phys., Polar Issue*, in press, 1993.

Dozier, J., and S.G. Warren, Effect of viewing angle on the infrared brightness temperature of snow, *Water Resour. Res.*, *18(5)*, 1424-1434, 1982.

Dutton, E.G., J.J. DeLuisi, and G. Herbert, Shortwave aerosol optical depth of Arctic haze measured on board the NOAA WP-3D during AGASP-II, April 1986, *J. Atmos. Chem.*, *9*, 71-79, 1989.

Francis, J., Improvements to TOVS retrievals over sea ice and their application to estimating Arctic energy fluxes, paper presented at *Third Conference on Polar Meteorology and Oceanography, Portland, Sept. 29 to Oct. 2, 1992,* Am. Meteorol. Soc., 25-28, 1992.

Hanel, G., The properties of atmospheric aerosol particles as functions of the relative humidity at thermodynamic equilibrium with the surrounding moist air, *Adv. Geophys.*, *19*, 73-188, 1976.

Herman, G.F., and J.A. Curry, Observational and theoretical studies of solar radiation in Arctic stratus clouds, *J. Clim. Appl. Meteorol.*, *23*, 5-24, 1984.

Heymsfield, A.J., and C.M.R. Platt, A parameterization of the particle size spectrum of ice clouds in terms of the ambient temperature and the ice water content, *J. Atmos. Sci.*, *41*, 846-855, 1984.

Hobbs, P.V., *Ice Physics*, Oxford University Press, New York, 1974.

Huschke, R.E., Arctic cloud statistics from air calibrated surface weather observations, *Memo. RM-6173-PR*, Rand Corp., Santa Monica, Calif., 1969.

Kahl, J.D., and A.D.A. Hansen, Determination of regional sources of aerosol black carbon in the Arctic, *Geophys. Res. Lett.*, *16,* 327-330, 1989.

Key, J., and R.G. Barry, Cloud cover analysis with arctic AVHRR data; 1, Cloud detection, *J. Geophys. Res.*, *94*(D15), 18,521-18,535, 1989.

Key, J., and M. Haefliger, Arctic ice surface temperature retrieval from AVHRR thermal channels, *J. Geophys. Res.*, *97*(D5), 5885-5893, 1992.

Key, J., and S. Peckham, Probable errors in width distributions of sea ice leads measured along a transect, *J. Geophys. Res.*, *96*(C10), 18,417-18,423, 1991.

Key, J., R. Stone, J. Maslanik, and E. Ellefsen, The detectability of sea ice leads in satellite data as a function of atmospheric conditions and measurement scale. *Ann. Glaciol.*, *17*, in press, 1993.

Kidder, S.Q., and H.-T. Wu, Dramatic contrast between low clouds and snow cover in daytime 3.7 µm imagery, *Mon. Weather Rev.*, *112*(11), 2345-2346, 1984.

Kneizys, F.X., E.P. Shettle, W.O. Gallery, J.H. Chetwynd, Jr., L.W. Abreu, J.E.A. Selby, R.W. Fenn, and R.A. McClatchy, Atmospheric transmittance/radiance: Computer code LOWTRAN 5, AFGL-TR-80-0067, *Environ. Res. Pap.*, *697*, 233 pp., Air Force Geophys. Lab., Bedford, Mass., 1980.

Kneizys, F.X., E.P. Shettle, W.O. Gallery, J.H. Chetwynd, L.W. Abreu, J.E.A. Selby, S.A. Clough, and R.W. Fenn, Atmospheric transmittance/radiance: computer code LOWTRAN 6, *AFGL-TR-83-0187* Air Force Geophys. Lab., Bedford, Mass., (Available as *NTIS AD A137796* from Natl. Tech. Inf. Serv., Springfield, VA.), 1983.

Kneizys, F.X., E.P. Shettle, L.W. Abreu, J.H. Chetwynd, G.P. Anderson, W.O. Gallery, J.E.A. Selby, and S.A. Clough, Users Guide to LOWTRAN 7, AFGL- TR-88-0177, *Environ. Res. Pap.*, *1010*, 137 pp., Air Force Geophys. Lab., Bedford, Mass., 1988.

Konig-Langlo, G., and A. Zachek, Radiation budget measurements over Antarctic sea ice in late winter, *World Climate Research Programme, Sea-Ice and Climate, Rep. WCRP-62, WMO/TD-442*, World Meteorol. Organ., Geneva, 1991.

Maykut, G.A., Large-scale heat exchange and ice production in the central Arctic, *J. Geophys. Res.*, *87*(C10), 7971-7984, 1982.

Mendonca, B.G., J.J. DeLuisi, and J.A. Schroeder, Arctic haze and perturbations in the solar radiation fluxes at Barrow, Alaska, paper presented at 4th Conference on Atmospheric Radiation, Am. Meteorol. Soc., Toronto, Ont., Canada, June 1981.

National Oceanic and Atmospheric Administration, *NOAA Polar Orbiter Data User's Guide*, U.S. Dept. of Commer., Natl. Oceanic and Atmos. Admin., Natl. Environ. Satellite, Data, and Inf. Serv., Feb. 1991.

Platt, C.M.R., and Harshvardhan, Temperature dependence of cirrus extinction: Implications for climate feedback, *J. Geophys. Res.*, *93*, 11,051-11,058, 1988.

Rahn, K.A., and R.J. McCaffrey, On the origin and transport of the winter Arctic aerosol, *Ann. N.Y. Acad. Sci.*, *338*, 486-503, 1980.

Rosen, H.T., T. Novakov, and B.A. Bodhaine, Soot in the Arctic, *Atmos. Environ.*, *15,* 1371-1374, 1981.

Rossow, W.B., L.C. Garder, and A.A. Lacis, Global, seasonal cloud variations from satellite radiance measurements, Part I; Sensitivity of analysis, *J. Clim.*, *2*, 419-458, 1989.

Sakellariou, N.K., H.G. Leighton, and Z. Li, Identification of clear and cloudy pixels at high latitudes from AVHRR radiances, *Int. J. Remote Sensing*, in press, 1992.

Schnell, R.C., R.G. Barry, M.W. Miles, E.L. Andreas, L.F.Radke, C.A. Brock, M.P. McCormick, and J.L. Moore, Lidar detection of leads in Arctic sea ice, *Nature*, *339,* 530-532, 1989.

Serreze, M.C., J.D. Kahl, and R.C. Schnell, Low-level temperature inversions of the Eurasian Arctic and comparisons with Soviet drifting station data, *J. Clim.*, *5(6)*, 599-613, 1992.

Shettle, E.P., and R.W. Fenn, Models of the aerosols of the lower atmosphere and the effects of humidity variations on their optical properties, *Rep. AFGL-TR-79-0214*, Air Force Geophys. Lab., Bedford, Mass, Sept. 17, 1979.

Shettle, E.P., F.X. Kneizys, S.A. Clough, G.P. Anderson, L.W. Abreu, and J.H. Chetwynd, Cloud models in LOWTRAN and FASCODE, paper presented at Cloud Impacts on DOD Operations and Systems 1988 Workshop, Silver Spring, MD., Oct. 18-20, 1988.

Smith, S.D., R.J. Anderson, G. den Hartog, D.R. Topham, and R.G. Perkin, An investigation of a polynya in the Canadian archipelago, 2, Structure of turbulence and sensible heat flux, *J. Geophys. Res.*, *88,* 2900-2910, 1983.

Stephens, G.L., The transfer of 3.7µm radiation through model cirrus clouds, paper presented at Fourth Conference on Atmospheric Radiation, Am. Meteorol. Soc., Toronto, Ont., Canada, June 1981.

Stone, R.S., Properties of austral winter clouds derived from radiometric profiles at the south pole, *J. Geophys. Res.*, in press, 1993.

Stone, R.S., G.L. Stephens, C.M.R. Platt, and S. Banks, The remote sensing of thin cirrus cloud using satellites, lidar and radiative transfer theory, *J. Appl. Meteorol.*, *29*, 353-366, 1990.

Stowe, L.L., C.G. Wellemeyer, T.F. Eck, H.Y.M. Yeh, and The Nimbus-7 Cloud Data Processing Team, Nimbus-7 global cloud climatology, Part I; Algorithms and validation, *J. Clim.*, *1*, 445-470, 1988.

Tsay, S.C., and K. Jayaweera, Physical characteristics of Arctic stratus clouds, *J. Clim. Appl. Meteorol.*, *23*, 584-596, 1984.

Tsay, S.C., K. Stamnes, and K. Jayaweera, Radiative energy budget in the cloudy and hazy Arctic, *J. Atmos. Sci.*, *46*(7), 1002-1018, 1989.

Valero, F.P.J., T.P. Ackerman, and W.J.Y. Gore, Radiative effects of the Arctic haze, *Geophys. Res. Lett.*, *10*(12), 1184-1187, 1983.

Valero, F.P.J., T.P. Ackerman, and W.J.Y. Gore, The effects of the Arctic haze as determined from airborne radiometric measurements during AGASP II, *J. Atmos. Chem.*, *9*, 225-244, 1989.

Vowinckel, E., and S. Orvig, The Climate of the North Polar Basin, in World Survey of Climatology, vol. 14, *Climates of the Polar Regions*, pp. 129-252, Elsevier, New York, 1970.

Wahiche, C., N.A. Scott, and A. Chedin, Cloud detection and cloud parameters retrieval from the satellites of the TIROS-N series, *Ann. Geophys.*, *4B*(2), 207-222, 1986.

Warren, S.G., C.J. Hahn, J. London, R.M. Chervin, and R.L. Jenne, Global distribution of total cloud cover and cloud type amounts over the oceans, DOE/ER-0406, *Tech. Note NCAR / TN-317+STR*, 42 pp. plus maps, Natl. Cent. for Atmos. Res., Boulder, Colo., Dec. 1988.

Yamanouchi, T., K. Suzuki, and S. Kawaguchi, Detection of clouds in Antarctica from infrared multispectral data of AVHRR, *J. Meteorol. Soc. Jpn*, *65*, 949-961, 1987.

J. R. Key and R.S. Stone, Division of Cryospheric and Polar Processes, Cooperative Institute for Research in Environmental Sciences, University of Colorado, Boulder, Colorado 80309-0449.

(Received September 3, 1992;
revised December 30, 1992;
accepted January 4, 1993.)